Model-based trajectory classification of anchored molecular motor-biopolymer interactions

John B. Linehan,[1] Gerald Alan Edwards,[1] Vincent Boudreau,[2,3] Amy Shaub Maddox,[1,*] and Paul S. Maddox[1,*]

[1]Department of Biology, University of North Carolina-Chapel Hill, Chapel Hill, North Carolina; [2]Department of Plant and Microbial Biology, University of California-Berkeley, Berkeley, California; and [3]Department of Biochemistry and Biophysics, University of California-San Francisco, San Francisco, California

ABSTRACT   During zygotic mitosis in many species, forces generated at the cell cortex are required for the separation and migration of paternally provided centrosomes, pronuclear migration, segregation of genetic material, and cell division. Furthermore, in some species, force-generating interactions between spindle microtubules and the cortex position the mitotic spindle asymmetrically within the zygote, an essential step in asymmetric cell division. Understanding the mechanical and molecular mechanisms of microtubule-dependent force generation and therefore asymmetric cell division requires identification of individual cortical force-generating units *in vivo*. There is no current method for identifying individual force-generating units with high spatiotemporal resolution. Here, we present a method to determine both the location and the relative number of microtubule-dependent cortical force-generating units using single-molecule imaging of fluorescently labeled dynein. Dynein behavior is modeled to classify trajectories of cortically bound dynein according to whether they are interacting with a microtubule. The categorization strategy recapitulates well-known force asymmetries in *C. elegans* zygote mitosis. To evaluate the robustness of categorization, we used RNAi to deplete the tubulin subunit TBA-2. As predicted, this treatment reduced the number of trajectories categorized as engaged with a microtubule. Our technique will be a valuable tool to define the molecular mechanisms of dynein cortical force generation and its regulation as well as other instances wherein anchored motors interact with biopolymers (e.g., actin, tubulin, DNA).

WHY IT MATTERS   Asymmetric cell division is critical for creating the different cell types that constitute a multicellular organism. To accomplish asymmetric division, molecular machinery within a cell must generate a force differential between the two cell poles. Determining the location and relative strength of force generators is important but difficult to do; the dense packing of force generators, such as dynein, on the surface confound detection of the force-generating population. To overcome this challenge, we developed a method to identify individual molecular units that contribute to force generation in the cell with high spatial and temporal resolution. This new approach will enable the study of the molecular regulation of force generation by anchored motor proteins and biopolymers in diverse cellular contexts.

INTRODUCTION

In the *C. elegans* embryo, polarity is established with the entry of the sperm nucleus and its associated centrioles during fertilization (1). Spindle positioning results from the integration of force-producing interactions between astral microtubules and dynein on the cortex.

During anaphase, the spindle is displaced into the embryo posterior due to higher magnitudes or numbers of microtubule pulling force events in the posterior (2−4). At the culmination of zygotic mitosis, this asymmetry leads to the division of the embryo into two differently sized daughter cells, which, via distinct mechanisms, also have different fates (5,6).

During zygotic prophase, the plus end of microtubules emanating from the centrosomes interact with tethering and force generation machinery at the cell cortex. Microtubule minus-end interactions with the maternal pronucleus, in coordination with the plus-end interactions at the cortex, result in centrosome separation, pronuclear migration, and spindle positioning (7−10).

The microtubule minus-end directed motor protein dynein is coupled to the plasma membrane via a cortical complex. This cortical complex consists of one pair of redundant heterotrimeric Gα subunits (GOA-1 and GPA-16) bound to the plasma membrane, the redundant go-loco proteins GPR-1 and -2, and the NuMA-like protein LIN-5. This coupling allows dynein to generate cortical pulling forces on microtubules (11−14). In this complex, dynein binds directly to LIN-5; its motor domain interacts with the plus ends of microtubules emanating from centrosomes (15,16). To transmit force from the cortex to microtubules and thus centrosomes, dynein either processively associates with the plus end of depolymerizing microtubules or pulls on microtubules by motoring toward the minus-ends anchored within the centrosomes, or performs a combination of both activities (17−20).

Light-sheet fluorescence microscopy and spinning disc confocal imaging of fluorescently labeled probes for the plasma membrane interpreted small invaginations as a proxy for the number of cortical force-generating units (21,22). A higher abundance of GPR1/2 and LIN-5 in the zygote posterior suggests that the force imbalance is due at least in part to there being more force-generating units in the posterior (12). The number of dynein molecules bound to LIN-5 complexes is greater in the posterior of anaphase-stage zygotes in comparison with the anterior (19). Fluorescence imaging of dynein at the cortex of anaphase-stage zygotes revealed that dynein exhibited either directed or diffusive-like behavior. Directed dynein trajectories were found in equal numbers throughout the zygote, while diffusive-like trajectories were asymmetrically distributed at the poles. Depletion of GPR1/2 via RNAi reduced the number of diffusive-like trajectories, indicating that diffusive trajectories make up the force-generating population (22). These findings support the model that asymmetric force generation results from an anisotropic distribution of force-generating units between the poles of the *C. elegans* zygote.

The location of cortical force generators has also been inferred from imaging microtubule plus ends at the cortex. Based on the lifetime of their appearance at the cortex, microtubule plus ends were classified as either pushing or pulling on the spindle, with the population associated with pulling spending less time at the cortex than the pushing group (23). While it is well accepted that there is an asymmetry in forces driving asymmetric division, these techniques fail to capture transient interactions that drive dynein behavior during mitosis. For instance, membrane invaginations require forces larger than individual dynein force-generating units, only capturing a subset of force-generation events (21,22). In addition, "diffusive-like" trajectories covers a broad range of behav-

iors that could encompass distinct pools of motion (behavior) within the population. Thus, a high-spatio-temporal-resolution analysis was needed to directly measure the behavior of single molecules of dynein.

We sought to define the behaviors of cortically located dynein. We used total internal reflection fluorescence microscopy (TIRFm) with a fluorescently tagged dynein heavy chain strain (eGFP::DHC-1, Schmidt et al. 2017) to detect dynein at the zygote cortex. Subsecond imaging rates and super-resolution positioning of the signal-generated trajectories represent spatial fluctuations of dynein over time. We developed a novel approach to categorize trajectories into those in which force-generation events did or did not occur. Trajectories were categorized by generating a motion model describing the movement of membrane-bound dynein at the cortex, termed the "swivel model." Using the model, we simulated dynein behavior in the presence and absence of a microtubule. These simulations resulted in quantitative predictions of dynein motion that were then compared to measured trajectory data. We were then able to classify trajectories according to the median value of the distribution of their displacements. Thus, we identified individual cortically bound dynein that interacts with a microtubule, and distinguished this from the cortically bound population that is not.

To determine the efficacy of our novel model-based trajectory classification method, we compared our categorization of dynein trajectories collected in the anterior and posterior of prophase- and anaphase-stage zygotes. We found that cortical force is higher in the anterior pole during prophase, and higher in the posterior pole in anaphase. We next assessed whether the model was indeed sensitive to the assumption that it can detect the presence of microtubules. In total, the swivel model-based trajectory classification method is sensitive to microtubule number, and concluded spatial- and cell-cycle-based differences in force generation that agreed with others' published findings (4,12,18,21−23). Future applications of our approach will be used to study the direct regulation of dynein and its role in cortical force generation at the *C. elegans* zygote cortex throughout mitosis.

MATERIALS AND METHODS

C. elegans culture, RNAi, and microscopy

The *C. elegans* strain SV1803 (he264[eGFP::dhc-1]) was maintained at 20°C using standard procedures (24) (Schmidt et al. 2017). Bacterial strains containing a vector expressing double-stranded RNA under the isopropyl β-ᴅ-1-thiogalactopyranoside-inducible promoter were obtained from the Ahringer library (Bob Goldstein's

laboratory, UNC-Chapel Hill). Targets were confirmed by sequencing.

Adult animals in the fourth larval stage (L4) were fed bacteria harboring the empty RNAi vector (L4440) as a negative control for 24 h before imaging or with bacteria expressing dsRNA targeting *tba*-2 for 16 h (longer TBA-2 depletion caused gross defects in oogenesis and zygote mitosis). Embryos were dissected from treated hermaphrodites and mounted in egg buffer between a no. 1.5 coverslip and a 4% agarose pad and sealed with VaLaP (25). Embryos were imaged in prophase or anaphase at anterior or posterior poles (64 μm^2) on a Nikon TIRF microscope with a 1.5× magnifier and a 100× Apo TIRF oil-immersion objective (NA = 1.49, Nikon), an Andor iXon3 EMCCD camera and NIS-Elements (Nikon) at 22°C. The incident angle of the laser was maximized to illuminate only the cortex of the embryo at anterior or posterior poles (64 μm^2). A custom emission light path was created that reduced the image pixel size to 60 nm. The pixel size was verified using a micrometer. An image was acquired every 27 ms.

Image analysis

A high density of dynein particles was observed at the cortex that confounded the identification of individual particles and trajectories. To account for the poor signal/noise ratio, we photobleached the specimens for 1000 time points (27 s). The photobleached frames were removed before processing. A histogram-matching photobleaching algorithm available in Fiji (26,27) was applied to decrease the variability of particle intensity and tracking segmentation over time. All image analysis was done using the TrackMate (28−30) plugin in Fiji (27). Tracking was performed using a difference of Gaussian detection segmenter (estimated object diameter = 0.4 μm, quality threshold = 6) and simple linear assignment problem tracking (linking max distance = 0.5 μm, gap-closing distance = 0.5 μm, gap-closing max frame gap = 1) (27,29,30). Tracks within 1 pixel of the edge of the image were discarded. Tracks with fewer than 5 spots were discarded from the categorization analysis (Table 1).

Calculation of turn angles

The direction taken of each step within a trajectory was determined as,

$$\phi_{turn} = \tan^{-1}\left(\frac{\Delta y}{\Delta x}\right)$$

where Δy is the distance between sequential y position coordinates within a trajectory, and Δx is the distance between sequential x position coordinates within a trajectory.

Protein size calculation

GOA-1, GPR1/2, and LIN-5 lengths were calculated from *C. elegans* predicted structures using AlphaFold (Jumper et al. 2021; Varadi et al. 2022). Cryo-EM structure of two dynein tail domains (*H. sapiens*) with BICD-2 (*M. musculus*) and dynactin (*S. scrofa*) were used from RSCB PDB to calculate the length of the force-generation complex (31,32). Protein length was estimated using the greatest linear distance between polar amino acids. The file IDs accessed for this study were PDB: 6F1T (Dynein complex), UPID: P45970 (LIN-5), UPID: P51875 (GOA-1), UPID: Q95QJ7 (GPR-1), UPID: Q03569 (GPR-2).

Swivel model description

In this section we describe the motion of membrane-anchored dynein using a mathematical model that considers the force-generation complex as a structure with geometry similar to a ball joint (Fig. 2). The first assumption of the model was that protein-protein and protein-membrane interactions within the complex do not turn over and remain fixed to the same position at the membrane relative to other cellular structures throughout the duration of a trajectory. We assumed that each of the component proteins of the complex stack is in series, forming a lever arm pointing 90°, perpendicular, to the membrane when at rest (Fig. 2 *A*).

We modeled the force-generation complex as a rigid rod whose tip is displaced along the surface of a

TABLE 1 Mitotic stage, zygote pole imaged, number of zygotes imaged, number of trajectories collected, and the number of trajectories categorized with swivel model-based classification strategy

Stage	Pole	Embryos	Tracks (5+ points)	Number of tracks categorized as free swivel	Number of tracks categorized as interacting swivel	Avg points per track/time (s)
Prophase	anterior	24	3538	2418	2159	8/0.22
Prophase	posterior	23	2160	1568	1286	7/0.19
Anaphase	anterior	13	3431	2369	1694	8/0.22
Anaphase	posterior	14	4012	2851	2102	8/0.22
Prophase *tba-2(RNAi)*	anterior	9	932	562	399	8/0.22
Prophase *tba-2(RNAi)*	posterior	6	622	375	210	8/0.22

hemisphere while the base remains fixed in the same location at the membrane. Thus, we expressed the position of the fluorescence molecule in the spherical coordinate system: the location of the fluorescence molecule was given by the position vector $r(\rho, \phi, \theta)$, where r is the position of the tip of the complex approximating the location of the green fluorescence molecule attached to dynein heavy chain, ρ is the length of the force-generation complex and dynein from tip to base, ϕ is the azimuthal angle, and θ is the polar angle (Fig. 2 B and C).

The variable θ is the deflection of the lever arm from the line perpendicular to the membrane and is proportional to the magnitude of the force applied to the complex causing its deflection. The magnitude of the external force acting on the lever arm was assumed to be governed by stochastic processes. The distribution of the magnitude of forces acting on the lever arm is represented as a Gaussian distribution for θ, $\theta_{external} = N(0, 0.34\theta_{max})$, where θ_{max} is the maximum angle of deflection from the line perpendicular to the membrane, to be determined (Fig. 2 B and C). The standard deviation of the polar angle Gaussian function is given by $0.34\theta_{max}$ since 68% of normally distributed values fall within plus or minus one standard deviation of the mean of the normal function. A Gaussian function is used because we assume that smaller magnitude forces, causing shallower deflections, are more likely to occur than are deeper deflections caused by larger magnitude forces. The external force causing deflection in the polar angle is opposed by a Hookean restoring force acting to push the force complex back to the vertical position, $\theta_{restore} = (0 - \theta_i)$. Since the force-generation complex falls within the regime of a low Reynolds number, the force balance equation is,

$$\theta_{i+1} = \theta_{external} + \theta_{restore} + \theta_i$$

$$\theta_{i+1} = \theta_{external} + (0 - \theta_i) + \theta_i$$

$$\theta_{i+1} = \theta_{external} \qquad (1)$$

The polar angle of the tip of the force-generation complex is given in time by the displacement caused by the external force.

The direction of the force acting on the lever arm is assigned by the azimuthal angle ϕ. We assume that the force is equally likely to push or pull the lever arm in any direction about the tail of the complex that is fixed to an immobile point in the membrane. This assumption is based on the distribution of azimuthal angles measured in the zygote in prophase and anaphase (Fig. 1, D–G). We represent the direction of a hypothetical force acting on the lever arm using a uniform distribution for the azimuthal angle ϕ, $\phi_{external} =$

$U(-\pi, \pi)$. The force is equally likely to act on the lever arm from any direction around the membrane-bound tail. The azimuthal angle is determined as

$$\phi_{i+1} = \phi_{external} + \phi_i . \qquad (2)$$

Displacement length probabilities

We assumed that all displacement lengths exist within the set $R, R = \{r_i \in r_1, r_2, r_3, ..., r_n\}$, then,

$$p(r_i) = P(R = r_i) \qquad (3)$$

$$p(r_i) = \frac{\int_i^n \delta(R - r_i)}{|R|} \qquad (4)$$

$$\Sigma_i\, p(r_i) = 1. \qquad (5)$$

This set provided the discrete probability function p for the probability of measuring r_i (33). Here, we bin displacement data by grouping values within a specified interval of displacement length. The set of displacement lengths R can be organized into subsets (bins) by subdividing the support of R into n intervals. The set $T = \{\tau_k \in \tau_1, \tau_2, \tau_3, ..., \tau_n\}$ contains disjoint subintervals, $\tau_k \cap \tau_{k+1} \cap ... \cap \tau_n = \{\varnothing\}$ (the bin intervals do not overlap) of the support. The set $M = \{m_k \in |\tau_1|, |\tau_2|, |\tau_3|, ..., |\tau_n|\}$ contains the cardinal of $\tau_i \in T$. The resulting adjusted probability mass function is,

$$p(\tau_k) = P(T = \tau_k) \qquad (6)$$

$$p(\tau_k) = \frac{m_k}{\Sigma_j m_j} \qquad (7)$$

$$\Sigma_k p(\tau_k) = 1 . \qquad (8)$$

This form was used to calculate the probability mass function for both simulated and experimentally measured displacements. Equations 6–8 are used to normalize the histograms used in this study for comparison across zygote poles and cell-cycle stages.

Monte Carlo simulation: Determining the maximum polar angle of deflection for both free swivel and interacting swivel models

A Monte Carlo simulation was performed to determine the maximum polar deflection angle θ_{max} for both free swivel and interacting swivel models (Fig. 2 B' and C'). This was done by simulating both models' behaviors
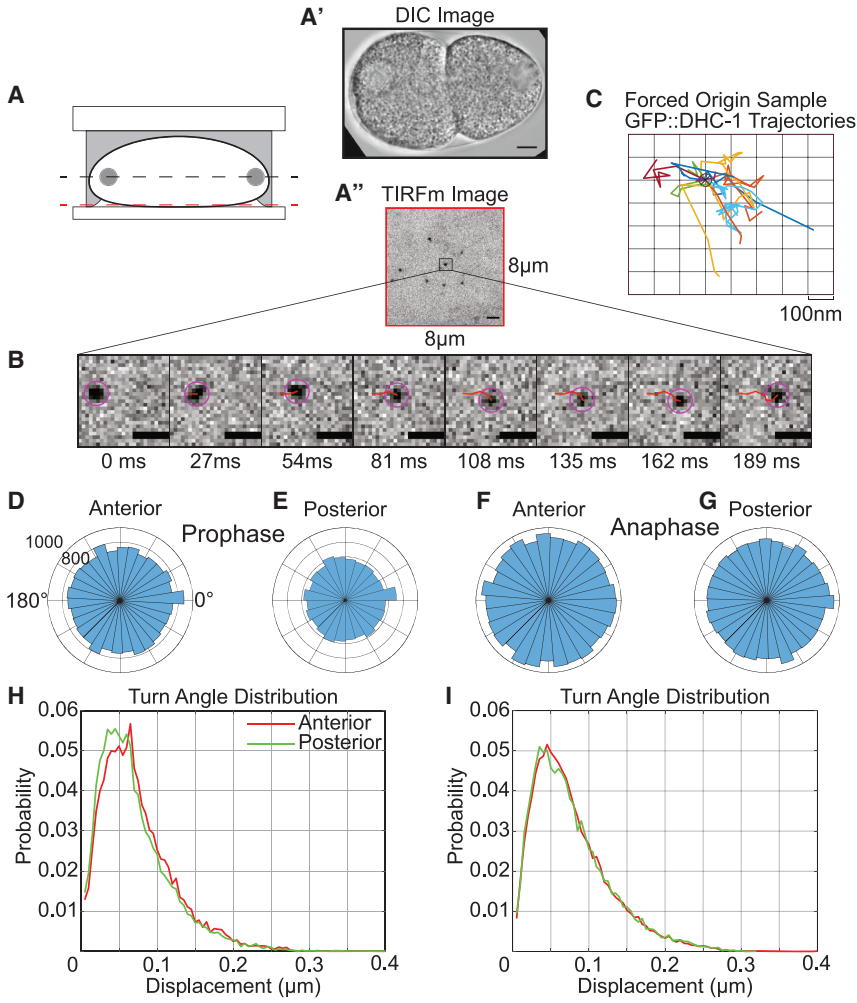
FIGURE 1 Schematic of zygote imaging and measured dynein kinetics. (A) Schematic of a prophase-stage *C. elegans* zygote compressed between 4% agarose (*gray*) and coverslip (*bottom*), indicating cytoplasmic (*black-dotted line*) and cortical (*red-dotted line*) focal planes. Cortical plane was imaged by total internal reflection fluorescence microscopy (TIRFm). (A') Prophase-stage zygote imaged using confocal-based DIC microscopy. (A'') Single representative TIRFm image of cortical eGFP-labeled dynein heavy chain (eGFP::DHC-1); contrast is inverted. Scale bars, 1 μm. (B) Montage of a dynein trajectory collected using TIRFm; red line indicates previous track positions. (C) Sample trajectories translated to a forced origin at zero. (D−G) Polar histogram of trajectory turn angles from all data per biological condition. (H−I) Probability mass function (distribution) of eGFP molecule displacements from all data per biological condition.

over the elements of the set of maximum polar angle of deflection θ', where $\theta' = \{\theta'_i \in 10, 15, 20, \ldots, 90\}$. We specify the maximum polar angle of deflection for the free swivel model $(\theta')^{free}$, selected from the set θ', and then simulated the interacting swivel model for each maximum polar angle of deflection in the set $(\theta')^{interacting} = \{(\theta')^{interacting}_i \in 10, 15, 20, \ldots, (\theta')^{free}\}$, thus $(\theta')^{interacting}$ is a subset of θ', $(\theta')^{interacting} \subseteq \theta'$, while $(\theta')^{free}$ was a single number (with the exception when $i = 1$, both free swivel and interacting swivel models are evaluated at 10° only). The value $(\theta')^{free}$ and the set $(\theta')^{interacting}$ together compose the parameters of one tranche of simulations.

For each element of θ' a Gaussian probability distribution function was calculated as,

$$f(\theta) = e^{\frac{-\theta^2}{2\sigma^2}} \tag{9}$$

where $\sigma = 0.33\theta'_i$ is the standard deviation of the distribution. Thus, $3\sigma \approx \theta'_i$, less than 0.1% of simulated po-

sitions exceed the maximum polar angle of deflection. The external force is taken to be the absolute value of Eq. 7, $\theta_{external} = \sqrt{f(\theta)^2}$. $\phi' = \{\phi'_i \in -\pi, -\pi+.1, \ldots, \pi\}$ defines all angular positions in the azimuthal plane that can be visited, where

$$g(\phi'_i) = \frac{1}{|\phi'|} \tag{10}$$

is the probability of a given ϕ'_i. Each angle ϕ'_i is equally likely to be selected. For a specified $(\theta'_i)^{free}$, a doppelganger style approach was adopted where each trajectory from every zygote was simulated using that trajectory's measured number of time points, such that the heterogeneity of track lengths is considered (33). Trajectory length likely encodes information regarding dynein binding time to the force-generation complex given the constraint that TIRF detects particles within roughly 200 nm of the zygote membrane. Since cortically bound dynein is anchored to the membrane, the trajectory length is largely uncorrelated with
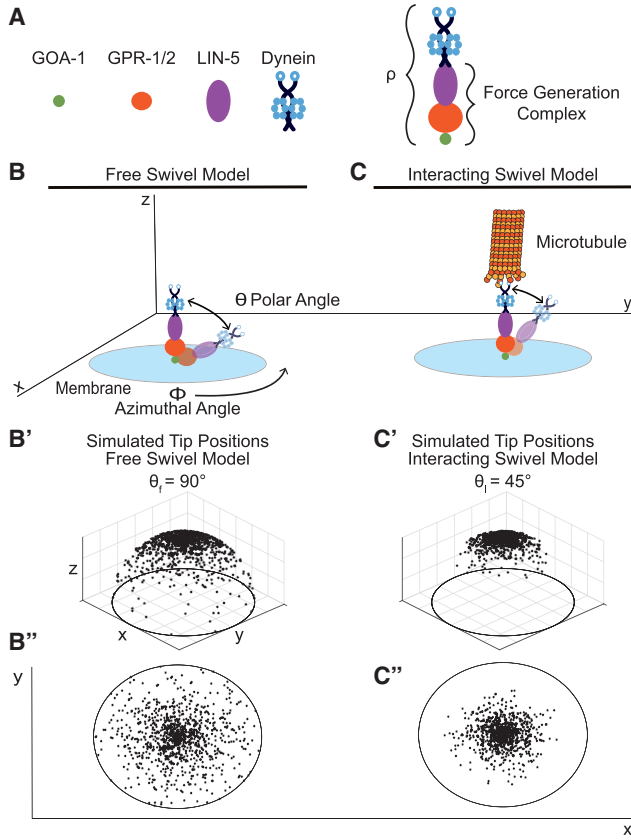
FIGURE 2 Force-generation complex and swivel model. (*A*) Proteins of the force-generation complex, dynein, and full force-generation complex with dynein (ρ). (*B*) Free swivel model: dynein and force-generation complex deflect off the line perpendicular to the membrane. (*C*) Interacting swivel model: depiction of force-generation complex and dynein interacting with a microtubule. (*B'* and *C'*) Simulation of free (*B'*) and interacting (*C'*) swivel model given arbitrary critical angles 90° (*B* and *B'*) and 45° (*C* and *C''*). Black dots: position of the simulated fluorescence label on the surface of a hemisphere viewed in perspective view (*B'* and *C'*) or top-down (*B''* and *C''*).

cytoplasmic diffusion, requiring that trajectory length be considered in the simulation.

Position coordinates are generated using angles from $f(\theta)$ and $g(\phi'_i)$ in Eqs. 1 and 2. The result of the simulation for the specified angle $(\theta'_i)^{free}$ is the vector $(\delta r)^{free}$ containing the distance between successive points in each simulated trajectory. The position of the simulated fluorescence molecule was mapped from spherical coordinates to cartesian coordinates using the transform equations

$$x = \rho \cos \phi \sin \theta \qquad (11)$$

$$y = \rho \sin \phi \sin \theta \qquad (12)$$

(34). The length between successive positions was calculated as,

$$\delta r_j = \left(\left(x_{j+1} - x_j\right)^2 + \left(y_{j+1} - y_j\right)^2 \right)^{\frac{1}{2}}. \qquad (13)$$

The vector $(\delta r)^{free}$ is of size (n_{sim} x 1), where n_{sim} was the number of displacements for a given condition's total trajectories (anterior prophase, posterior prophase, anterior anaphase, posterior anaphase).

For each $(\theta'_i)^{free}$ there were *i* elements in the set $(\theta')^{interacting}$, where each element was simulated as above, resulting in the set

$$\overline{\delta r^{interacting}} = \left\{ (\delta r)_i^{interacting} \in (\delta r)_1^{interacting}, (\delta r)_2^{interacting}, \right.$$

$$\left. (\delta r)_3^{interacting}, \dots, (\delta r)_{\left|(\theta')^{interacting}\right|}^{interacting} \right\}$$

where each $(\delta r)_i^{interacting}$ contains the doppelganger simulation of measured trajectories. The tranche of simulations ran for $(\theta')^{free}$ results in the set ω containing the concatenated displacements from both free swivel and interacting swivel models,

$$\boldsymbol{\omega} = \left\{ \omega_i \in \left[(\delta r)^{free}, (\delta r)_1^{interacting} \right], \dots, \right.$$

$$\left. \left[(\delta r)^{free}, (\delta r)_{\left|(\theta')^{interacting}\right|}^{interacting} \right] \right\}$$

For each $\omega_i \in \boldsymbol{\omega}$ an adjusted probability mass function for displacement length was generated (Eqs. 4–6),

$$p(\boldsymbol{\omega}) = \left\{ p(\omega_i) \in p(\omega_1), p(\omega_2), p(\omega_3), \dots, p\left(\omega_{\left|(\theta')^{interacting}\right|}\right) \right\}$$

The sum of square error is taken to determine how well each $p(\omega_i) \in p(\boldsymbol{\omega})$ generated from every tranche of simulation fits the displacement probability mass function determined for each condition (Table 1). The measured displacement probability mass function is given by $p(\tau)$. The sum of squared errors is determined as,

$$SSE^{pole,mitotic\ stage} = \Sigma_k \left(p\left(\omega_i^{n,k} \right) - p(\tau_k)^{pole,mitotic\ stage} \right)^2 \qquad (14)$$

For a single tranche of the simulation that specified the value $(\theta)^{free}$ and the set $(\theta)^{interacting}$, where $\rho(\tau)^{pole,mitotic\ stage}$ is the probability mass function for the step length of each pole and mitotic stage condition from the single-particle localizations collected using TIRFm. The average of the sum of square error for each condition is taken.

$$SSE = < SSE^{anterior,prophase} \quad SSE^{posterior,prophase}$$

$$SSE^{anterior,anaphase} \quad SSE^{posterior,anaphase} >$$

where <> indicates averaging. The minimal error parameterization was saved for each tranche $(\theta)^{free}$.

The parameter combination, $[(\theta)^{free}, (\theta)_i^{interacting}]$, with the minimal average sum of square error value is taken as the best fit. The whole simulation structure was replicated 10 times, and the optimal parameterization of each replicate was saved. The minimum and maximum values of both swivel models' replicate simulations are taken to give the range of angles. So that the maximum angle of deflection for the free swivel model falls within the bounds,

$$\theta_{max}^{free} - \delta < \theta_{max}^{free} < \theta_{max}^{free} + \delta$$

Similarly for the interacting swivel model,

$$\theta_{max}^{interacting} - \delta < \theta_{max}^{interacting} < \theta_{max}^{interacting} + \delta$$

where the maximum degree of deflection for both free swivel and interacting swivel models are given as an angular band. Since the fluorescent molecule moves about the surface of a hemisphere, the resulting step length distributions for the interacting swivel group will be similar regardless of the orientation of the microtubule relative to the force-generation complex.

Trajectory categorization metrics, determination of percentile values

The swivel model displacement probability mass functions generated using the best fitting polar angles of deflection for both models were statistically characterized using the sum of square error. Simulation of the swivel model results in quantitative predictions of the statistical behavior of membrane-anchored dynein over time; in both the presence or the absence, of a microtubule. The displacement probability mass functions for both free swivel and interacting swivel models are characterized by percentile. The 25th and 75th percentile values of both swivel models' simulated displacement length probability mass functions comprise the upper and lower limits of the interval of displacement lengths acceptable for classification as either model. To determine the percentiles of the set of values δr, we first sorted the elements of δr into ascending order, $\delta r_1 < \delta r_2 < \delta r_3 < \ldots < \delta r_N$. The 25th and 75th percentile is determined as,

$$n = \frac{P}{100} * N$$

where P is 25 or 75, respectively, and n is the index number of the element of δr, the displacement value of the corresponding percentile.

Determining the overlap of the swivel model's displacement probability mass functions (likelihood of improperly classifying a trajectory)

The likelihood that a trajectory was misclassified as belonging to either swivel model was determined by calculating the percentage overlap of the free swivel and interacting swivel models. The 25th percentile value of the free swivel model displacement probability mass function overlaps the 75th percentile value of the interacting swivel model displacement probability mass function (see Fig. 5). Since displacement probability mass functions are discrete, we took the sum of the value of the probability mass functions over the interval in which the two overlap,

$$\Delta^{free} = \sum_{i}^{\delta r(n_{25})^{free} < \delta r < \delta r(n_{75})^{interacting}} P(\delta r_i)^{free}$$

Similarly, the interacting swivel model

$$\Delta^{Interacting} = \sum_{i}^{\delta r(n_{25})^{free} < \delta r < \delta r(n_{75})^{interacting}} P(\delta r_i)^{interacting}$$

is the percentage overlap. We adjusted the probability mass function by organizing data using the same subintervals (Eqs. 4–6). The percentage overlap Δ for both swivel models is in general calculated as

$$\Delta = \sum_{k}^{\tau(n_{25})^{free} < \tau < \tau(n_{75})^{interacting}} P(\tau_k) \quad (15)$$

where $\tau_k = r_k' - \delta \leq (\delta r_i \in \delta r) < r_k' + \delta$. We then determined the percentage overlap of both models varying the upper percentile of the free swivel and interacting swivel group (the lower percentile was set to the 25th percentile value) from the 26th to the 75th percentile. The percentage overlap was calculated for each interval and is used to score the confidence of the categorization. Overlap values over 20% are considered highly likely to be improperly classified.

Brownian motion simulation

The motion of a particle undergoing Brownian diffusion was simulated to determine the 25th percentile value of its step length distribution in time. A probability step length function was generated in the form,

$$p(t) = exp\left(-\frac{\left(\frac{x^2}{4Dt}\right)}{2\sqrt{\pi Dt}}\right)$$

where x is the support of the distribution, $-0.8\ \mu m < x < 0.8\ \mu m$, t is the time between an image taken by

the TIRFm microscope $t = 0.027$ s, and D is the diffusion coefficient measured previously by Ananthanarayanan et al. (35), adjusted for the sampling rate of 37 images per second $D = \frac{0.0173\mu m}{0.027s}$. The simulation consisted of 1000 trajectories containing 16 positions, each with coordinates given in (x, y). The displacements within each trajectory were calculated for each trajectory. The simulated trajectory displacements were concatenated into a single distribution, and the 25th percentile was determined as above.

Testing position coordinate coupling: Bootstrapping and one-way analysis of variance

The swivel model assumes the constraint that the x and y coordinates of the single-particle localizations are coupled (Eq. 16). The model-based classification was performed where each trajectory's position coordinates were randomly permuted (shuffled). The shuffled trajectories' displacements were calculated, and the trajectory was classified. This was done for every trajectory measured using TIRFm. This procedure was performed in the anterior and posterior of prophase- and anaphase-stage zygotes.

Control data generated using the bootstrapping method were statistically compared with the number of dynein particles categorized by the swivel model in each biological context assessed using a one-way analysis of variance (ANOVA) test to compare the experimentally measured categorization numbers and the bootstrapped control data numbers to determine whether the means of the two groups are statistically significantly different from one another (one-way ANOVA, MATLAB [ANOVA1]).

Numerical programming

All programming was performed in MATLAB version 9.9.0.1857802 (R2020b).

RESULTS

Membrane-anchored dynein motion is spatially symmetric and conserved across mitotic stages in the *C. elegans* zygote mitosis

Cortically generated forces are required for asymmetric cell division of the *C. elegans* zygote. The molecular motor dynein binds to microtubules to generate cortical forces. Cortically associated dynein may or may not interact with a microtubule, which could create distinct pools of dynein motion. It is unknown if dynein exhibits a distinct form of motion (i.e., trajectory) when bound to the membrane in both the absence and presence of a microtubule.

Dynein is bound to the membrane via the force-generation complex, consisting of redundant membrane-bound Gα protein (GOA-1/GPA-16), GPR1/2, and LIN-5, while engaged in force generation (2,15). To determine the form of motion of membrane-anchored dynein engaged in force generation during mitosis, it was necessary to use imaging techniques with high spatiotemporal resolution.

We visualized dynein with a dynein heavy-chain green fluorescently tagged fusion protein (24). The enhanced green fluorescent protein (eGFP) has a length of 4 nm and a width of 2 nm (37). The fluorescent label is sufficiently close to, within 4 nm of, the dynein heavy chain for the fluorescent label to provide an accurate readout of the dynein location including consideration of the resolution limit of TIRFm (see materials and methods). In addition, an image was collected at roughly 27 ms intervals (~37 frames/s), allowing us to observe dynein's transient interactions with microtubules and the cortex throughout a trajectory, while optimizing the tradeoff between signal/noise ratio and acquisition speed.

To determine the form of dynein motion when engaged in force generation at the cortex, we first collected images of dynein at both zygote poles in prophase and anaphase stages of mitosis, when microtubule-based cortical forces are required. We used single-particle imaging of the *C. elegans* zygote by TIRFm to image dynein behavior during cortical force generation, which revealed numerous dynein trajectories at the cortex (36) (see materials and methods; Fig. 1, A–A″, B, and C; Video S1). Trajectories were visibly distinguishable based on shape, with most trajectories seemingly crossing over the same point repeatedly, while others moved persistently in a single direction (Fig. 1 C).

To study the kinetics of dynein engaged in cortical force generation, it was necessary to statistically characterize the subpopulations of dynein trajectories collected using TIRFm. To quantify the impression that trajectories largely crossed through the same point, we next compared the distribution of azimuthal turn angles (direction of a turn in the (x, y) plane). We found that every angle was visited an equal number of times among these four conditions (Fig. 1, D, E, F, and G). This indicated that the fluorescent molecule attached to the dynein heavy chain was equally likely to move in any direction in the (x, y) plane, and that the form of motion of membrane-anchored dynein is conserved across the zygote spatially and in terms of cell-cycle stage.

We next looked to determine the motility of cortically located dynein. For clarity, here both displacement and step length are used to refer to the distance between successive points within a trajectory collected using TIRFm, and not to the processivity of dynein along a microtubule. To do so, we measured the step length

that dynein takes between successive positions within a trajectory. We generated probability mass functions describing step length for each pole and mitotic stage (Fig. 1, *H* and *I*). We found that dynein is most likely to take a short step ($40 - 60 \, nm/27 \, ms$) in both stages of mitosis and at either pole. This indicated that the fluorescent label's displacement over the timescale of image acquisition is within the length of a single pixel (60 nm). Together, the turn angle (Fig. 1, *D−G*) and displacement probability data (Fig. 1, *H* and *I*) suggested that the location of the fluorescent label described a region around a single central point, likely the location where the force-generation complex is bound to the membrane. The statistical characterization of dynein kinetics at the cortex was the same across zygote poles and cell-cycle stages, indicating that the behavior of individual dynein molecules is the same across these spatiotemporal scales. This means that a single motion model is sufficient to describe membrane-anchored dynein behavior in zygotic mitosis.

Mechanistic motion model of membrane-anchored dynein

To interpret trajectory information, and to identify the population of dynein engaged in force generation, we set out to generate a model of dynein motion. Our model was informed by both our observations of trajectory shapes and our statistical characterization of the population data (Fig. 1). A general overview of the mechanistic motion model of membrane-anchored dynein follows (see materials and methods for a comprehensive description of the model).

We assumed that the force-generation complex is a rigid rod, referred to as the lever arm, which extends perpendicular to the membrane (Fig. 2 *A*). The model posits that the lever arm is free to move both horizontally and vertically about the point where it is bound to the cortex, so that the force-generation complex and dynein swivel about a fixed point in space. The location of the GFP-tagged dynein when bound to the cortex through the force-generation complex is modeled using a spherical coordinate system, with position coordinates (ρ, θ, ϕ). ρ is the radial coordinate, defined as the tip-to-tail length of the force-generation complex and dynein (Fig. 2 *A*). θ is the polar angle that measures the degree of deflection from the line perpendicular to the cell membrane, and ϕ is the azimuthal angle that describes a position in the (x, y) plane. Thus, the membrane-bound force-generation complex is free to swing across a full circle in the azimuthal angle $\phi \, \epsilon \, [-\pi, \pi]$ (Fig. 2, *B* and *C*). The position of the fluorescent tag, given by $\boldsymbol{r}(\rho, \phi, \theta)$, is constrained to the surface of a hemisphere (Fig. 2, *B'* and *C'*).
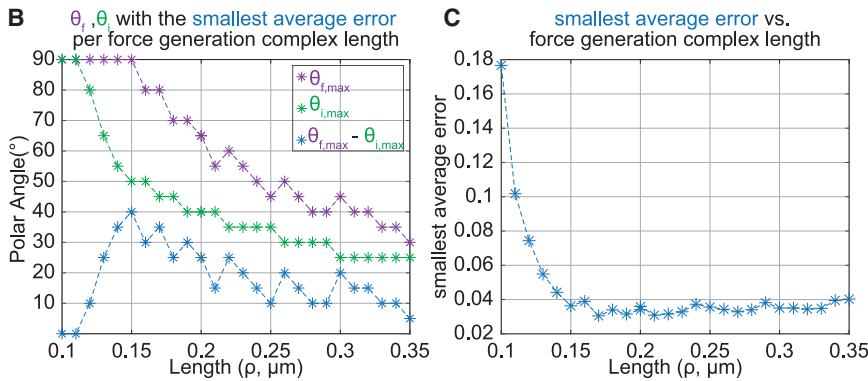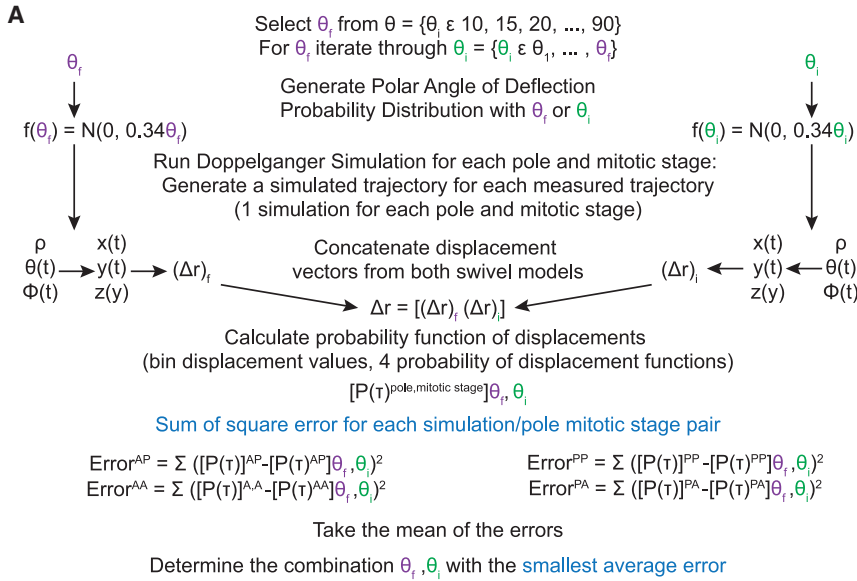
The motion model provides a theoretical framework to predict the statistical characteristics of cortically located dynein trajectories in the case where membrane-anchored dynein is interacting with a microtubule. We predicted that microtubule interactions stabilize the orientation of the force-generation complex, constraining the motility of the lever arm so that the fluorescent molecule explores a smaller section of the hemisphere (Fig. 2, *C'* and *C''*). By contrast, in the absence of a microtubule, the lever arm does not experience a stabilizing force, and stochastic forces from the cytoplasmic milieu allow the fluorescent molecule to explore the entire surface of a hemisphere (Fig. 2, *B'* and *B''*).

We refer to our motion model of dynein as the swivel model. Dynein that is cortically bound through the force-generation complex and interacts with a microtubule is called the *interacting swivel* group (Fig. 2, *C−C''*). Dynein that is bound to the force-generation complex but not interacting with a microtubule is the *free swivel* group (Fig. 2, *B−B''*). Simulation data for the free swivel group (Fig. 2 *B'*) and interacting swivel group (Fig. 2 *C'*) illustrate the impact on step length of two different maximum polar angles of deflection. The difference in the area explored between the two models is clear in 2D as well (Fig. 2, *B''* and *C''*). The free swivel group has a larger polar angle of deflection; the fluorescent molecule is found within a relatively larger area of a hemisphere (Fig. 2, *B'* and *B''*). In comparison, the interacting swivel model posits that microtubule interactions constrain the fluorescent label to a smaller area of the hemisphere, resulting in a decreased maximum polar angle of deflection (Fig. 2, *C'* and *C''*). Thus, our experiment regarding membrane-anchored dynein motion resulted in a quantitatively testable hypothesis of dynein motility that we later test against measured data.

Dynein-microtubule interactions stabilize force-generation complex orientation in silico

TIRFm imaging of fluorescently labeled dynein in *C. elegans* zygotes revealed the trajectories of membrane-associated dynein and provided numerical characterization of the motion of the molecular motor in time. Since dynein is differentially enriched, regulated, and activated with respect to spatial landmarks and cell-cycle phases (12), the trajectories likely captured dynein in diverse behaviors at the cortex. To categorize the thousands of trajectories generated using high-spatiotemporal-resolution imaging (Table 1), we used our parameter-based mathematical model of dynein motion at the cortex.

The swivel model predicts that the measured displacement length distribution can be explained using

A

Select θ_f from $\theta = \{\theta_i \, \varepsilon \, 10, 15, 20, ..., 90\}$
For θ_f iterate through $\theta_i = \{\theta_i \, \varepsilon \, \theta_1, ..., \theta_f\}$

θ_f θ_i

Generate Polar Angle of Deflection
Probability Distribution with θ_f or θ_i

$f(\theta_f) = N(0, 0.34\theta_f)$ $f(\theta_i) = N(0, 0.34\theta_i)$

Run Doppelganger Simulation for each pole and mitotic stage:
Generate a simulated trajectory for each measured trajectory
(1 simulation for each pole and mitotic stage)

ρ x(t)   Concatenate displacement   x(t) ρ
$\theta(t) \rightarrow$ y(t) $\rightarrow (\Delta r)_f$ vectors from both swivel models $(\Delta r)_i \leftarrow$ y(t) $\leftarrow \theta(t)$
$\Phi(t)$ z(y)   z(y) $\Phi(t)$

$\Delta r = [(\Delta r)_f \, (\Delta r)_i]$

Calculate probability function of displacements
(bin displacement values, 4 probability of displacement functions)

$[P(\tau)^{\text{pole,mitotic stage}}]\theta_f, \theta_i$

Sum of square error for each simulation/pole mitotic stage pair

$\text{Error}^{AP} = \Sigma \, ([P(\tau)]^{AP} - [P(\tau)^{AP}]\theta_f, \theta_i)^2$ $\text{Error}^{PP} = \Sigma \, ([P(\tau)]^{PP} - [P(\tau)^{PP}]\theta_f, \theta_i)^2$
$\text{Error}^{AA} = \Sigma \, ([P(\tau)]^{A,A} - [P(\tau)^{AA}]\theta_f, \theta_i)^2$ $\text{Error}^{PA} = \Sigma \, ([P(\tau)]^{PA} - [P(\tau)^{PA}]\theta_f, \theta_i)^2$

Take the mean of the errors

Determine the combination θ_f, θ_i with the smallest average error

B θ_f, θ_i with the smallest average error per force generation complex length

C smallest average error vs. force generation complex length

FIGURE 3 Simulation flow chart and determination of force-generation complex size. (A) Outline of simulation procedure to determine the best fitting parameter combination of angles to describe the data measured. (B) Determination of the optimal length of simulated force-generation complex bound to dynein. For each value of force-generation complex length (lever arm, ρ), the resulting maximum angles of deflection are plotted (green and purple lines). Blue: difference in the maximum angle of deflection values for free swivel and interacting swivel models. (C) The average sum of squared error of $\theta_{f,max} - \theta_{i,max}$ generated in (B).

two values of a single parameter: the maximum angle of deflection for both the free swivel and interacting swivel groups. An outline of the simulation follows. The swivel model posits that the lever arm can bend no more than 90° from the line perpendicular to the membrane. Thus, we evaluated the simulation over angles starting from 10° to 90° in 5° increments. The *interacting swivel* model was evaluated for each angle from 10° up to the specified free swivel maximum polar angle (see materials and methods, Fig. 3 A). The simulated free swivel and interacting swivel groups' step length distributions were concatenated. The set of step lengths for the two groups were combined so that a probability mass function of step length could be calculated for the total simulated population. The sum of squared error was used to determine the similarity between simulated and measured step length.

The swivel model has three parameters, ρ, θ^{free}, $\theta^{interacting}$ that were determined by comparison of simulated displacement data to measured displacement data. The simulation steps listed above (Fig. 3) detail the method used to determine the best fitting polar an-

gles of deflection for both swivel models. To determine the value of the parameter ρ, the length of the force-generation complex and dynein, we iterated over lengths from 100 to 350 nm, determining which theoretical value provided both an optimal goodness of fit and angular resolution between swivel models (Fig. 3, B and C; angular resolution is defined as $\theta_{max}^{free} - \theta_{max}^{interacting}$, the difference in the maximum degree of deflection of the polar angle from free and interacting swivel models). We found that suggested values for the force-generation complex and dynein length below 110 nm provided neither a good fit nor angular resolution between models (Fig. 3, B and C). Both angular resolution and error improved as the force-generation complex length increased, with angular resolution reaching a maximum at $\rho = 150$ nm. As the value of the force-generation complex length increased beyond 150 nm, angular resolution decreased, and error stabilized. As the force-generation complex length increased past 300 nm the maximum polar angles of deflection approached convergence, and the error grew (Fig. 3, B and C).

The simulation data indicated that the optimal parameterization value for the force-generation complex and dynein length was $\rho = 150$ nm, which provided both optimal angular resolution and error. We next looked to determine whether this optimal parameterization value presented a reasonable estimate of the true length of the force-generation complex and dynein. We made a second estimate of the value for ρ using predicted structural data (see materials and methods). The globular protein Gα is the smallest protein in this complex with an estimated diameter of 11 nm. GPR1/2 consists of two subunits, GPR-1 and GPR-2, that are modeled here as having a total diameter of 12 nm. LIN-5 is a coiled-coil protein that binds to GPR1/2 and dynein, it is estimated to be 33 nm long (Fig. 2 A). Dynein length is estimated to be 56 nm (Fig. 2 A; see materials and methods for protein radius and length estimates). In total, we calculate that the force-generation complex from tip to tail, consisting of Gα, GPR1/2, LIN-5, and dynein, is 113 nm long (Fig. 2 A). The GFP label is attached to the dynein heavy chain, which we estimated to be located roughly 30 nm from the location where dynein binds to LIN-5 (19). Thus, the linear distance from the membrane bound GOA-1 to the GFP molecule is roughly 90 nm. The theoretically optimal value of force-generation complex and dynein length, $\rho = 150$ nm is within one pixel length greater than the estimate generated by 3D reconstruction data. These estimates for the length of the force-generation complex and dynein are in close agreement, and together indicate that the length of the *C. elegans* force-generation complex and dynein is likely between 110 and 150 nm.

We next ran multiple iterations of the simulation with the specification that $\rho = 150$ nm. The parameterization with the smallest average sum of square error was taken as the maximum angle of deflection for the free swivel model; the angular width was $\theta_f = [80°, 90°]$ for the free swivel group, and $\theta_I = [50°, 55°]$ for the interacting swivel group (Fig. 4 A). The step length distribution functions for each pole and stage were generated by concatenating their respective simulations for free swivel and interacting swivel using the best fitting angles from both models (Fig. 4, B−E). The theoretical curves in Fig. 4, B−E contained the simulated displacement lengths between positions given angles $\theta = 50, 55, 80, 85, 90$. Simulation data generated for each pole and mitotic stage had best fits in this same angular range, indicating that dynein kinetics are conserved across poles and mitotic stages in the worm zygote.

Statistical characterization of model-based classification efficacy

The step length probability mass function of both free swivel and interacting swivel groups was determined
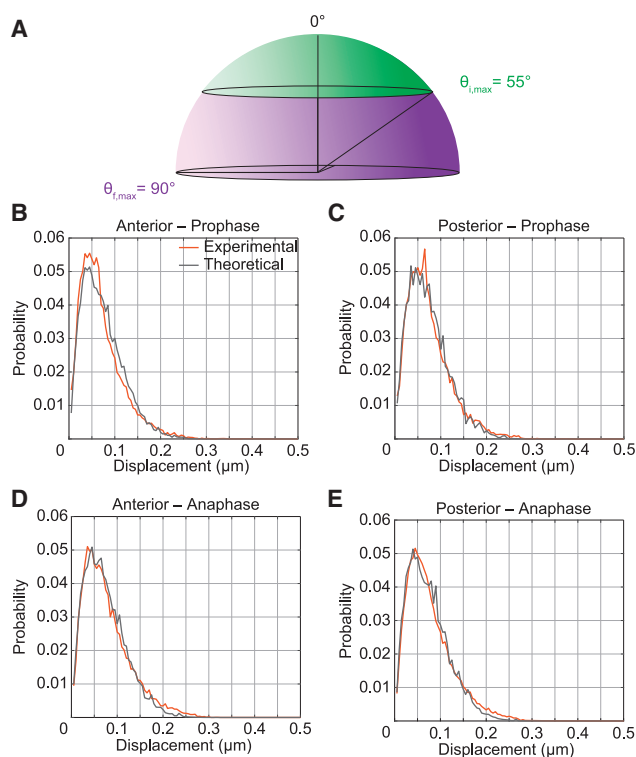

FIGURE 4 Maximum angles of deflection. (*A*) Schematic of the area of a hemisphere where the eGFP molecule is most likely to be found when 1) a microtubule is present, and the force-generation complex is engaged in force generation (*green area*), or 2) in the absence of a microtubule (*purple area* and *green area*). The area in which the eGFP molecule can explore is greater in the absence of a microtubule than in its presence. (*B−E*) Overlay of model-based simulation step length probability mass functions, determined by concatenating the step length distributions for the conditions $\theta = 50, 55, \ldots 80, 85, 90$ with the experimentally measured step length distributions from each pole and mitotic stage.

by Monte Carlo simulation (38) (see materials and methods). The 25th and 75th percentile values were the minimum and maximum values of step length to classify a trajectory as belonging to either the free swivel or interacting swivel groups (Fig. 5, A and B). The 75th percentile of the interacting swivel group overlaps with the 25th percentile of the free swivel group (Fig. 5 C).

Determining the uncertainty in trajectory classification is a necessary step to isolate the population of force-generating dynein at the cortex throughout the mitotic cell cycle, and provides a rigorous metric to interpret swivel model-based classifications in the context of cell-cycle stages. The space in which the fluorescent molecule could be found was encoded into the trajectory by the linear distance between sequential positions. The space explored by the fluorescent molecule of membrane-anchored dynein in the free swivel model not only included, but was greater than, the area explored by the fluorescent molecule in the interacting swivel model.
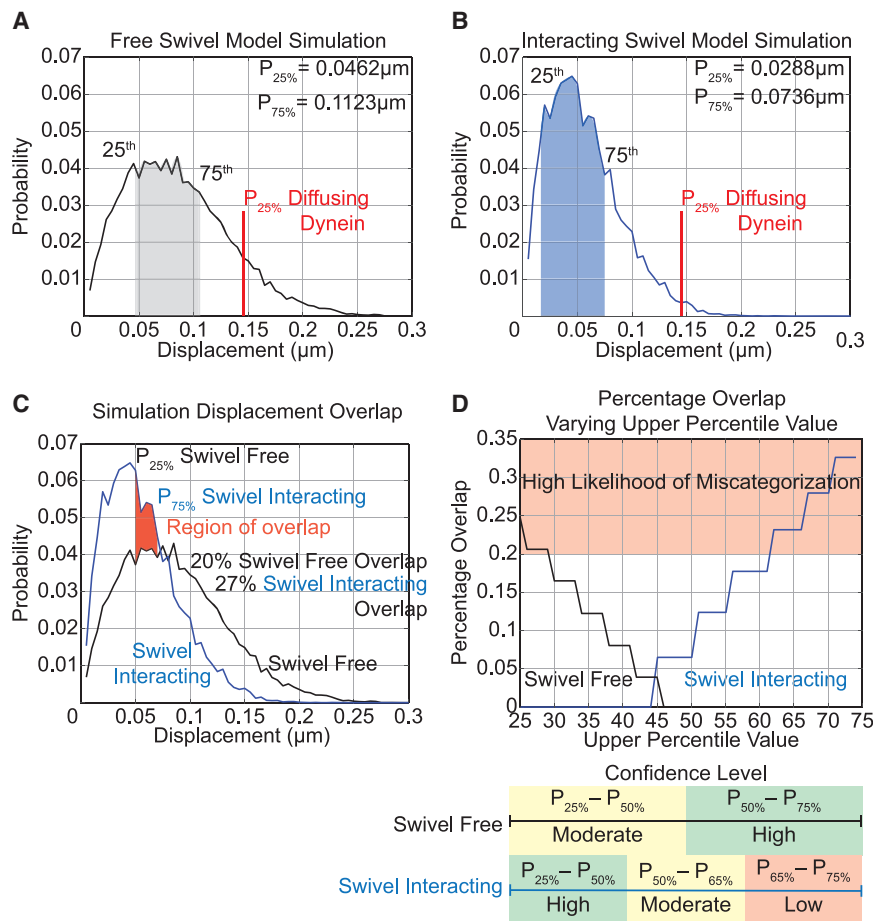
FIGURE 5 Statistical characterization of step length probability functions for free swivel and interacting swivel models. (*A*) Probability step length function for simulated free swivel group, containing the concatenated theoretical model step lengths of angles ranging from 80 to 90°. The 25th and 75th percentile values ($P_{i\,\%}$) indicate the range of acceptable values to be classified as free swivel. The red line marks the 25th percentile step length of a theoretical dynein protein undergoing Brownian diffusion at the cortex. (*B*) Probability step length function for simulated interacting swivel dynein trajectories, generated from concatenated step length distributions with maximum angles of deflection of 50 and 55°. The 25th and 75th percentile values indicate the range of acceptable values to be classified as interacting swivel. Red: as in (*A*). (*C*) Overlay of free swivel and interacting swivel probability mass function of displacement length (step length). (*D*) Percent overlap of the two probability mass functions for different percentile values. Below: confidence level classifications.

We found that 20% of the free swivel step length distribution overlaps with the interacting swivel distribution. Similarly, 27% of the interacting swivel step length distribution overlaps with the free swivel distribution (Fig. 5 *C*). The overlap percentages of the two models indicate a poor level of confidence (over 20% overlap; Fig. 5 *D*). We evaluated the percentage overlap over the 25th to 75th percentile values of the free swivel and the interacting swivel model's step length distribution. In doing so we can further divide the percentile window into subintervals based on confidence in the categorization. The free swivel model had high confidence in categorization for median values of measured trajectory step length that fall within its 50th to 75th percentile values, and we were generally confident in the categorizations falling within the 25th to 50th percentiles (overlap percentage greater than 20%). Conversely, we were highly confident of categorizations made of trajectories whose median step length is between the 25th and 50th percentile values of the interacting swivel model (Fig. 5 *D*), and confident in categorizations made of median

step lengths between the 50th and 65th percentile, and have low confidence for categorizations made in the 65th to 75th percentile (Fig. 5 *D*). Categorizations from both models are subdivided into confidence regimes (Fig. 6).

It is possible that dynein molecules undergoing diffusion penetrate the actomyosin cortex, contributing signals to the trajectory data set. To ensure that this population was not counted in the number of force-generating swivel interacting trajectories, we ran simulations of dynein undergoing Brownian diffusion near the cortex using a step length distribution generated with a previously reported value for cytoplasmic dynein diffusion (35). The median step length for dynein undergoing Brownian motion is 0.22 μm, while the 25th and 75th percentile values, used for categorization, are 0.14 and 0.31 μm. The 25th percentile range of diffusing dynein step lengths is greater than the 75th percentile value of the free swivel model (0.1123 μm). The likelihood of classifying a dynein molecule that is undergoing Brownian diffusion near the cortex as being bound to the cortex is significantly low so it is ignored (Fig. 5, *A* and *B*). In
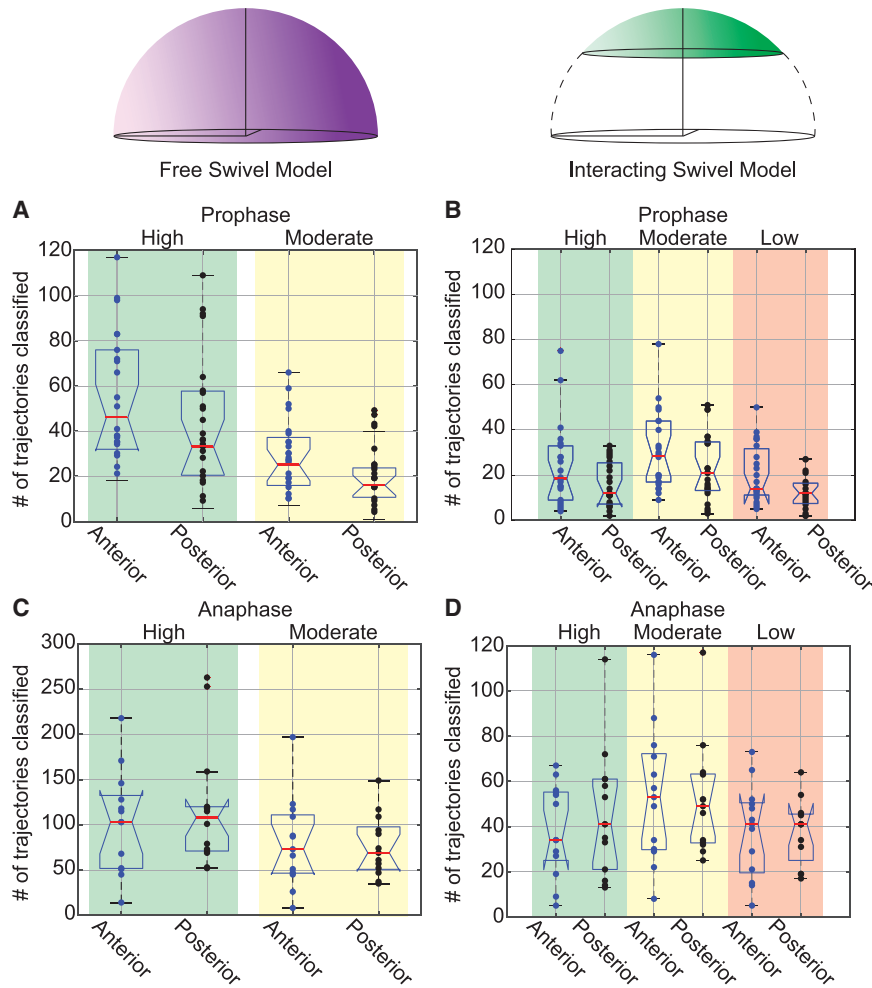
FIGURE 6 Application of the swivel model-based classification to measured single-particle dynein trajectories at the anterior and posterior of prophase- and anaphase-stage *C. elegans* zygotes. (*A* and *C*) Classifications of free swivel trajectories in posterior and anterior poles of prophase (*A*)- and anaphase (*C*)-stage zygotes, broken down by confidence in classification. (*A*) High-confidence free swivel categorizations in the anterior pole of prophase-stage zygotes (mean ± SD); 55 ± 29, moderate confidence 28 ± 16. High-confidence free swivel categorization in the posterior pole of prophase-stage zygotes 44 ± 30, moderate confidence categorizations 19 ± 13. (*C*) High-confidence free swivel categorizations in the anterior pole of anaphase-stage zygotes, 102 ± 57; moderate confidence 80 ± 50. High-confidence free swivel categorizations in the posterior pole of anaphase-stage zygotes, 118 ± 67; moderate confidence 76 ± 34. (*B* and *D*) Classifications of interacting swivel trajectories in posterior and anterior poles of prophase (*B*)- and anaphase (*D*)-stage zygotes, broken down by confidence in classification. (*B*) High-confidence interacting swivel categorizations in the anterior pole of prophase-stage zygotes, 24 ± 18; moderate confidence 30 ± 17; low confidence 20 ± 13. High-confidence interacting swivel categorization in the posterior pole of prophase-stage zygotes, 16 ± 10, moderate confidence 23 ± 15, poor confidence 12 ± 7. (*D*) High-confidence interacting swivel categorizations in the anterior of anaphase-stage zygotes 38 ± 20; moderate confidence 53 ± 29; and low confidence 38 ± 20. High-confidence interacting swivel categorizations in the posterior of anaphase-stage zygotes, 45 ± 27; moderate confidence 51 ± 24; low confidence 38 ± 14.

addition to our simulation data, we propose the following calculation to detail the difference in expected step lengths between diffusing dynein and cortically bound dynein. A rough approximation shows that cytoplasmic dynein undergoing Brownian motion with diffusion coefficient value $\frac{0.64\mu m^2}{s}$ (35), imaged at a sampling rate of roughly 37 frames per second, will have an expected diffusion coefficient per frame of $\frac{0.017\mu m^2}{sampling\ interval}$. Since the diffusion coefficient is a measure of area explored per unit of time, the square root of the value provides distance over time, or $\sqrt{0.017} \approx \frac{0.135\mu m}{sampling\ interval}$, which is a displacement in one dimension. Thus, the displacement vector $\delta r_b \approx \sqrt{0.135^2 + 0.135^2} \approx \frac{0.186\mu m}{sampling\ interval}$ has a value greater than the 75th percentile of the free swivel model. Taken together, these results indicate that it is unlikely that dynein undergoing diffusion at the cortex would be misclassified as cortically bound by either swivel model.

Swivel model-based trajectory classification recapitulates polar force asymmetries in prophase- and anaphase-stage *C. elegans* zygotes

After fertilization in the *C. elegans* zygote, the sperm-derived centrioles coordinate centrosome and pronuclear migration and centrosome/nuclear centration by transmitting cortically generated forces through microtubules (2,3). During prophase, the anterior end of the zygote has a greater amount of the force-generation components LIN-5 and GPR1/2 than the posterior, so it could be predicted that, during this phase of the cell cycle, microtubules reaching the anterior cortex undergo more force-generating events (and are therefore in the "interacting" group) than those extending to the posterior cortex (12).

We tested this idea by first categorizing each dynein single-molecule trajectory as free or interacting, and then subdividing trajectories by classification confidence (Fig. 5 *D*). The number of dynein trajectories

categorized as interacting swivel with high confidence was higher in the anterior (mean $\pm$ SD; 24 ± 4) than in the posterior (16 ± 2) (Fig. 6 *B*). The same trend held for trajectories with moderate and low confidence (Fig. 6 *B*). This finding supported the idea of a force asymmetry in the prophase of the first mitotic division in *C. elegans* (12). Interestingly, the numbers of trajectories categorized as belonging to the free swivel group with high and with moderate confidence were both also higher for the anterior than the posterior (high-confidence classifications: anterior 55 ± 6; posterior 44 ± 6) (Fig. 6 *A*). This finding is consistent with other reports of higher total numbers of cortical dynein molecules in the anterior (12).

In anaphase, higher abundance and activation of cortical dynein in the embryo posterior leads to locally higher pulling forces, asymmetric positioning of the spindle toward the posterior, and, ultimately, asymmetric cell division (2,4,12) . Since the difference in the cortex-based polar forces is slight in anaphase, we next tested whether our method of classifying single-particle dynein trajectories could distinguish these populations of cortically bound dynein at this stage. Trajectories classified with high confidence in the interacting swivel group reflect the previously identified asymmetry in the number of force-generating units in the embryo during anaphase (anterior 39 ± 6; posterior 45 ± 7). The total number of trajectories classified as the free swivel model of motion recapitulate this ratio as well (anterior 102 ± 16; posterior 118 ± 18). In total, the swivel model's categorization reflects that the posterior end generates a greater force in the anaphase zygote, but that the magnitude of the asymmetry is only slight.

Testing swivel model assumptions: Trajectory localization coordinates are correlated, and the swivel model is sensitive to the presence of microtubules

Here, we introduce a model to describe the behavior of a GFP molecule attached to a dynein heavy chain bound to the membrane by the cortical force-generation complex. The swivel model states that the position of the GFP particle localization is constrained to the surface area of a hemisphere. For this to be true the following constraint must be satisfied,

$$\rho(t) = \sqrt{x(t)^2 + y(t)^2 + z(t)^2} = constant \qquad (16)$$

That the total length of the force-generation complex and dynein is constant throughout the trajectory places a constraint on the relationship between the *x*, *y*, and *z* coordinates in time (Eq. 16). Thus, the position coordinates *x*, *y*, and *z* are highly correlated. If the

swivel model accurately describes the mechanism of the motion of cortically bound dynein, then random permutation of the position coordinates *x* and *y* within a trajectory in time would result in statistically significantly different distributions of classified trajectories in comparison with the unperturbed data. If the swivel model does not describe membrane-anchored dynein motion, then the permutation of *x* and *y* position coordinates in time will result in statistically indistinguishable distributions of trajectories classified by the swivel model.

To test the assumption that the length of the force-generation complex and dynein constrains the position of the single-particle localizations, we randomly permuted the *x* and *y* position coordinates of every measured trajectory, from both poles of prophase- and anaphase-stage zygotes. The displacements of the randomly permuted trajectories were calculated and classified by the swivel model. We found that the numbers of permuted trajectories classified in each pole and mitotic stage by both swivel modes were statistically significantly different from the numbers from our original data in seven out of eight conditions (Fig. 7, *A* and *B*). The one exception was that the number of permuted trajectories classified as a free swivel in the posterior of prophase zygotes was statistically indistinguishable from the number of unperturbed trajectories classified in time-ordered trajectories (Fig. 7 *A*). These results indicate that the *x* and *y* positions of single-particle localizations are highly correlated in the poles of prophase and anaphase *C. elegans* zygotes. This analysis thus supports the idea that membrane-anchored dynein swivels about a fixed point in space in a manner that satisfies the model constraint (Eq. 16) and that the swivel model is an accurate description of membrane-anchored dynein motion at the cortex.

A second assumption of the swivel model of membrane-anchored dynein is that dynein movement is sensitive to the presence of microtubules. To test this assumption, we depleted the microtubule subunit α-tubulin 2 (TBA-2). Microtubules are made up of dimers consisting of α- and β-tubulin proteins (39). We partially depleted α-tubulin protein (expected 30% reduction in protein) to avoid the pleiotropic defects resulting from more thorough depletions. The median number of interacting swivel trajectories classified in the anterior of the prophase stage was substantially lower in *tba-2(RNAi)* zygotes than in controls (9 zygotes, 440 trajectories; Fig. 7, *C* and *D*). The median number of trajectories classified as a free swivel in the anterior prophase was slightly lower in *tba-2(RNAi)* zygotes than controls (Fig. 7 *D*). In the posterior of prophase zygotes, the median number of trajectories classified as interacting swivel was lower in *tba-2(RNAi)* zygotes than in controls (6 zygotes, 305 trajectories; Fig. 7 *C*). The median
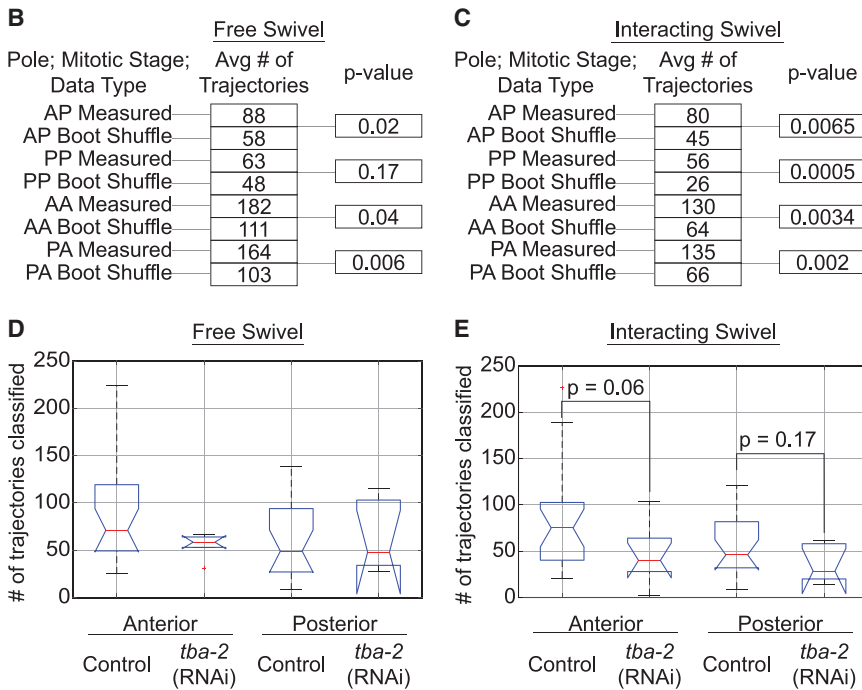
A The Constraint, $\rho^2 = x^2 + y^2 + z^2$, implies that coordinate values are coupled
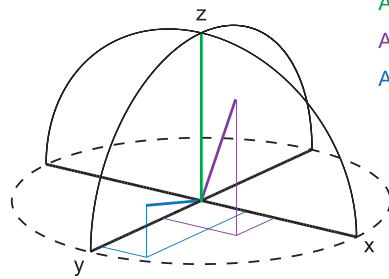
As z increases, x and y decrease

As x increases, y and z decrease

As y increases, x and z decrease

B Free Swivel

Pole; Mitotic Stage; Data Type	Avg # of Trajectories	p-value
AP Measured	88	
AP Boot Shuffle	58	0.02
PP Measured	63	
PP Boot Shuffle	48	0.17
AA Measured	182	
AA Boot Shuffle	111	0.04
PA Measured	164	
PA Boot Shuffle	103	0.006

C Interacting Swivel

Pole; Mitotic Stage; Data Type	Avg # of Trajectories	p-value
AP Measured	80	
AP Boot Shuffle	45	0.0065
PP Measured	56	
PP Boot Shuffle	26	0.0005
AA Measured	130	
AA Boot Shuffle	64	0.0034
PA Measured	135	
PA Boot Shuffle	66	0.002

FIGURE 7 Evaluation of swivel model assumptions. (*A*) Schematic of coordinate constraints on the position of a particle occupying a point in a semisphere. (*B* and *C*) Results of pairwise comparisons of measured and bootstrapped data for each cell pole and mitotic phase and model (one-way ANOVA). (*D* and *E*) The number of trajectories categorized as free (*D*) or interacting (*E*) swivel per stage zygote in control (L4440) and *tba-2* (RNAi) worms (one-way ANOVA).

D Free Swivel

E Interacting Swivel

number of trajectories categorized as a free swivel in the posterior of prophase was essentially unchanged by *tba-2(RNAi)* (Fig. 7 *D*). Together, these data indicate that the swivel model is sensitive to the presence of microtubules interacting with dynein.

DISCUSSION

We present a motion model to describe the behavior of cortically bound dynein as a function of whether it is interacting with a microtubule. In our model, interaction with microtubules reduces the degree to which the force-generation complex and dynein can deflect from a line perpendicular to the cell membrane. Our high-spatiotemporal-resolution image data of cortically located dynein using TIRF imaging strongly support this model.

We determined the maximum angle of deflection for both free swivel and interacting swivel groups by simulating trajectories and fitting the model-generated probability mass functions to imaging data. The best-fitting parameterizations indicate that cortically bound dynein protrudes perpendicular to the membrane into the actin cortex. Stochastic forces act on cortically bound dynein to reposition it; we speculate that the force-generation complex experiences a restoring force that increases as a function of the degree of deflection, which biases its position to perpendicular to the membrane. We speculate that, when interacting with a microtubule, the force-generation complex and dynein move about the surface of a hemisphere as dynein binds and unbinds microtubules, while simultaneously experiencing stochastic forces. Together with the above-mentioned restoring force, the affinity of dynein for the microtubule constrains the degree of deflection from perpendicular. Upon application of the model to categorize cortical dynein trajectories, we found that model classification recapitulates previously identified asymmetries in force generation during prophase (4,12,18,21).

In prophase-stage zygotes we observed a roughly twofold increase in both free swivel and interacting swivel trajectories in the anterior relative to the posterior. Our categorization technique identified a larger number of both free swivel and interacting swivel trajectories in anaphase than in prophase. The model identified a spatial asymmetry in anaphase: more free swivel trajectories were identified in the posterior of the embryo than in the anterior. The number of trajectories classified with high confidence as being engaged with a microtubule, the interacting swivel group, was slightly higher in the zygote posterior than the anterior (Fig. 6 C).

Statistical and biological testing of swivel model assumptions

A core assumption of the swivel model is that the position coordinates of the particle localization are highly correlated in time due to the constraint that the length of the force-generation complex and dynein is fixed (Eq. 16). We tested this assumption by randomly permuting trajectory position coordinates in time and comparing the number of trajectories categorized in both permuted and nonpermuted data (Fig. 7, A and B). We found that, in seven out of eight conditions, the number of trajectories classified by the swivel model was statistically significantly different, adding to the model's validity that membrane-anchored dynein motion is well described in the swivel model. The results of characterizing dynein movement in embryos with reduced microtubules also supported the idea that our model can distinguish cortically bound dynein that is interacting with a microtubule from dynein that is not.

We further tested the assumption that the swivel model is sensitive to the presence of microtubules by depleting the conserved microtubule subunit tba-2. We found that the number of trajectories classified as interacting swivel decreased in comparison with control (Fig. 7 B). We did not identify a decrease in the number of trajectories categorized as free swivel, as expected since microtubules are not required for dynein binding to the force-generation complex. These data indicate that the swivel model-based categorization method is indeed sensitive to the presence of microtubules.

Transient membrane-anchored dynein-microtubule interaction as the mechanistic unit of cortical force generation

The mechanism of cortical force generation in the worm zygote is often described as exerting a nearly constant force throughout cell-cycle events, such as the positioning of the mitotic spindle (4,18,21−23).

Previous work used laser ablation to cut the mitotic spindle in anaphase, after which spindle fragment recoil velocity was measured. The authors used a two-state model that directly related the number of force-generating units to the average speed of spindle fragments after optically induced centrosome disintegration. These results indicated the presence of roughly 50 cortical force-generating units responsible for the positioning of the zygote mitotic spindle, and that the posterior end likely contains a slightly greater part of that number due the spindle's eccentric position. Indeed, the authors calculated that there is an average of 1.42 force generators per spindle fragment in the anterior and 2.15 in the posterior (4). These results suggested that force-generating units are asymmetrically distributed about the zygote cortex and that there are far more astral microtubules reaching out to the cortex than there are force-generating units (18). Measurements of spindle recoil velocity after laser ablation provide information about the net force acting on the spindle without specification of the superimposed components that determine the net force magnitude. Indeed, the two-state model used in Grill et al. (4) posits that the net force from the cortex could result from the superposition of many individual units, but the measured retraction velocity does not provide this information directly. Spindle fragment retraction velocity results from a single constant force that was exerted at the time of ablation. Another study posited that the number of force-generating units acting on the mitotic spindle is at least 80 in the posterior end of the zygote based on the appearance of membrane invaginations attributed to a membrane-anchored molecular motor pulling along a microtubule (21). This methodology only detected force-generation events that persisted for a sufficiently long time for the protrusion to be detected. While these studies provided insight into cortical force generation integrated by the spindle (4), and considering the entire cortex (21), they relied on assumptions of the force-generating unit itself, and implied that the number of active force generators was a limiting factor. Our single-particle tracking and trajectory classification of cortically located GFP-labeled dynein indicated that dynein transiently binds microtubules continuously in both prophase and anaphase (mean trajectory lifetime was roughly 0.2 s), agreeing that a relatively higher number of force-generating units leads to force asymmetry. However, because astral microtubules must intersect a cortically bound dynein for force generation to occur, our data instead support the notion that a high density of force-generation complexes exist at the cortex, and that there is a greater number of force generators relative to the number of astral microtubules.

The discrepancy between our data and previous work led us to explore the relationship between astral microtubule-cortical dynein interaction and force generation. Extrapolating from the number of dynein molecules observed in our 64 μm^2 imaging area to the 1413 μm^2 polar surface area using our high-confidence classifications, we expect that a minimum of 848 membrane-anchored dynein-microtubule interactions occur per minute during chromosome segregation in the anterior end, and roughly 1002 in the posterior end, during anaphase. Our calculations of cortical force-generating units are 10–28 times greater than previous estimates; this discrepancy likely reflects that our work considers the action of all detectable cortical force generators over 1 min of time (4,21). A simplistic approximation is that the number of force generators exerting force on the centrosome is at least 18 per second in the posterior (using only our high-confidence-group classifications), or 49 force generators, according to calculations using all confidence groups for interacting swivel classifications. We posit that the net force acting on the spindle fragments in Grill et al. (4) resulted from numerous transient dynein-microtubule interactions that were integrated over time and experienced by the spindle as a roughly constant force. Indeed, we found that the average lifetime of interacting swivel dynein trajectories was 0.2 s. We measured only those dynein molecules that were within the imaging depth accessible by TIRFm, and were thus unable to directly measure the population of force-generating microtubule interactions that led to membrane invagination as observed in Redemann et al. (21). Our data set contains trajectories with lifetimes similar to those required for the formation of membrane invaginations identified in Redemann et al. (21), but those events are predicted to comprise only a fraction of the total number of trajectories measured at the cortex. Together, our data indicate that asymmetric force applied to the centrosome emerges as a result of many short-lived force-generation events that are exerted on microtubules by cortically located membrane-anchored dynein.

While our data reveal that a greater relative number of short-lived force-generating events can lead to force asymmetry, a higher rate of membrane-anchored dynein-microtubule interactions could also be explained by a higher cortical binding rate as proposed previously (22). We compared dynein trajectory length as a proxy for binding rate between the anterior and posterior poles of anaphase-stage zygotes, and found no statistical difference between the groups, failing to support that first hypothesis. Rather, we observe a higher total number of dynein particles in the posterior end of anaphase zygotes. To further scrutinize our results, we compared our data from prophase, where asymmetry of force generation is thought to be reversed (12). Our measurements predict that 643 membrane-anchored dynein-microtubule interactions occur in the anterior pole of the zygote during prophase and that 355 membrane-anchored dynein-microtubule interactions occur in the posterior pole. Our results from anaphase and prophase are consistent with previous findings quantifying cortical levels of LIN-5 and GPR 1/2 during mitosis, demonstrating a reversal of force generation asymmetry distribution from anterior in prophase to posterior in anaphase (12). In all, our data indicate that asymmetry in cortical force generation is a consequence of asymmetric distribution of dynein at the cortex rather than locally regulated and varying dynein cortical binding rate.

In sum, our novel model of cortically bound dynein behavior, which recapitulates the well-known force asymmetries in the *C. elegans* zygote, allowed us to classify cortically bound dynein as engaged or free. Future work will leverage this model to specifically study cortically bound dynein without confounding effects of considering cortically diffusing dynein. Beyond this application, our model will be of use to numerous studies of single-molecule localization, including investigation of myosin motors and chromatin-modeling machinery as they transiently bind to their substrates.

SUPPORTING MATERIAL

AUTHOR CONTRIBUTIONS

A.E. and V.B. designed and carried out experiments in *C. elegans* embryos and performed image and data analysis. J.B.L. designed the model and wrote MATLAB-based code used for data calculations, statistics, and computational modeling. J.B.L., A.E., V.B., A.S.M., and P.S.M. wrote the manuscript.

ACKNOWLEDGMENTS

DECLARATION OF INTERESTS

The authors declare no competing interests.

REFERENCES

1. Goldstein, B., and S. N. Hird. 1996. Specification of the antero-posterior axis in Caenorhabditis elegans. *Development.* 122:1467–1474. https://doi.org/10.1242/dev.122.5.1467.

2. Rose, L., and P. Gönczy. 2014. Polarity establishment, asymmetric division and segregation of fate determinants in early C. elegans embryos. *Worm* 1–43. https://doi.org/10.1895/wormbook.1.30.2.

3. Galli, M., and S. van den Heuvel. 2008. Determination of the cleavage plane in early C. elegans embryos. *Annu. Rev. Genet.* 42:389–411. https://doi.org/10.1146/annurev.genet.40.110405.090523.

4. Grill, S. W., J. Howard, …, A. A. Hyman. 2003. The distribution of active force generators controls mitotic spindle position. *Science.* 301:518–521. https://doi.org/10.1126/science.1086560.

5. Morrison, S. J., and J. Kimble. 2006. Asymmetric and symmetric stem-cell divisions in development and cancer. *Nature.* 441:1068–1074. https://doi.org/10.1038/nature04956.

6. Nance, J. 2005. PAR proteins and the establishment of cell polarity during C. elegans development. *Bioessays.* 27:126–135. https://doi.org/10.1002/bies.20175.

7. Gönczy, P., S. Pichler, …, A. A. Hyman. 1999. Cytoplasmic dynein is required for distinct aspects of MTOC positioning, including centrosome separation, in the one cell stage Caenorhabditis elegans embryo. *J. Cell Biol.* 147:135–150. https://doi.org/10.1083/jcb.147.1.135.

8. De Simone, A., and P. Gönczy. 2017. Computer simulations reveal mechanisms that organize nuclear dynein forces to separate centrosomes. *Mol. Biol. Cell.* 28:3165–3170. https://doi.org/10.1091/mbc.E16-12-0823.

9. Goldstein, B. 2000. Embryonic polarity: a role for microtubules. *Curr. Biol.* 10:R820–R822. https://doi.org/10.1016/s0960-9822(00)00790-9.

10. Robinson, J. T., E. J. Wojcik, …, T. S. Hays. 1999. Cytoplasmic dynein is required for the nuclear attachment and migration of centrosomes during mitosis in Drosophila. *J. Cell Biol.* 146:597–608. https://doi.org/10.1083/jcb.146.3.597.

11. Lorson, M. A., H. R. Horvitz, and S. van den Heuvel. 2000. LIN-5 is a novel component of the spindle apparatus required for chromosome segregation and cleavage plane specification in Caenorhabditis elegans. *J. Cell Biol.* 148:73–86. https://doi.org/10.1083/jcb.148.1.73.

12. Park, D. H., and L. S. Rose. 2008. Dynamic localization of LIN-5 and GPR-1/2 to cortical force generation domains during spindle positioning. *Dev. Biol.* 315:42–54. https://doi.org/10.1016/j.ydbio.2007.11.037.

13. Srinivasan, D. G., R. M. Fisk, …, S. van den Heuvel. 2003. A complex of LIN-5 and GPR proteins regulates G protein signaling and spindle function in C elegans. *Genes Dev.* 17:1225–1239. https://doi.org/10.1101/gad.1081203.

14. Gotta, M., Y. Dong, …, J. Ahringer. 2003. Asymmetrically distributed C. elegans homologs of AGS3/PINS control spindle position in the early embryo. *Curr. Biol.* 13:1029–1037. https://doi.org/10.1016/s0960-9822(03)00371-3.

15. Nguyen-Ngoc, T., K. Afshar, and P. Gönczy. 2007. Coupling of cortical dynein and G alpha proteins mediates spindle positioning in Caenorhabditis elegans. *Nat. Cell Biol.* 9:1294–1302. https://doi.org/10.1038/ncb1649.

16. Couwenbergs, C., J. C. Labbé, …, M. Gotta. 2007. Heterotrimeric G protein signaling functions with dynein to promote spindle positioning in C. elegans. *J. Cell Biol.* 179:15–22. https://doi.org/10.1083/jcb.200707085.

17. Kozlowski, C., M. Srayko, and F. Nedelec. 2007. Cortical microtubule contacts position the spindle in C. elegans embryos. *Cell.* 129:499–510. https://doi.org/10.1016/j.cell.2007.03.027.

18. Grill, S. W., and A. A. Hyman. 2005. Spindle positioning by cortical pulling forces. *Dev. Cell.* 8:461–465. https://doi.org/10.1016/j.devcel.2005.03.014.

19. Schmidt, R., L.-E. Fielmich, …, S. van den Heuvel. 2017. Two populations of cytoplasmic dynein contribute to spindle positioning in C. elegans embryos. *J. Cell Biol.* 216:2777–2793. https://doi.org/10.1083/jcb.201607038.

20. Gönczy, P. 2002. Mechanisms of spindle positioning: focus on flies and worms. *Trends Cell Biol.* 12:332–339. https://doi.org/10.1016/s0962-8924(02)02306-1.

21. Redemann, S., J. Pecreaux, …, J. Howard. 2010. Membrane invaginations reveal cortical sites that pull on mitotic spindles in one-cell C. elegans embryos. *PLoS One.* 5, e12301. https://doi.org/10.1371/journal.pone.0012301.

22. Rodriguez-Garcia, R., L. Chesneau, …, J. Pécréaux. 2018. The polarity-induced force imbalance in Caenorhabditis elegans embryos is caused by asymmetric binding rates of dynein to the cortex. *Mol. Biol. Cell.* 29:3093–3104. https://doi.org/10.1091/mbc.E17-11-0653.

23. Bouvrais, H., L. Chesneau, …, J. Pécréaux. 2021. The coordination of spindle-positioning forces during the asymmetric division of the Caenorhabditis elegans zygote. *EMBO Rep.* 22, e50770. https://doi.org/10.15252/embr.202050770.

24. Heppert, J. K., A. M. Pani, …, B. Goldstein. 2018. A CRISPR Tagging-Based Screen Reveals Localized Players in Wnt-Directed Asymmetric Cell Division. *Genetics.* 208:1147–1164. https://doi.org/10.1534/genetics.117.300487.

25. Wernike, D., C. van Oostende, and A. Piekny. 2014. Visualizing neuroblast cytokinesis during C. elegans embryogenesis. *J. Vis. Exp.* 51188 https://doi.org/10.3791/51188.

26. Miura, K. 2020. Bleach correction ImageJ plugin for compensating the photobleaching of time-lapse sequences. *F1000Res.* 9:1494. https://doi.org/10.12688/f1000research.27171.1.

27. Schindelin, J., I. Arganda-Carreras, …, A. Cardona. 2012. Fiji: an open-source platform for biological-image analysis. *Nat. Methods.* 9:676–682. https://doi.org/10.1038/nmeth.2019.

28. Tinevez, J.-Y., N. Perry, …, K. W. Eliceiri. 2017. TrackMate: An open and extensible platform for single-particle tracking. *Methods.* 115:80–90. https://doi.org/10.1016/j.ymeth.2016.09.016.

29. Ershov, D., M.-S. Phan, …, J.-Y. Tinevez. 2021. Bringing TrackMate in the era of machine-learning and deep-learning. Preprint at bioRxiv. https://doi.org/10.1101/2021.09.03.458852.

30. Ershov, D., M.-S. Phan, …, J.-Y. Tinevez. 2022. TrackMate 7: integrating state-of-the-art segmentation algorithms into tracking pipelines. *Nat. Methods.* 19:829–832. https://doi.org/10.1038/s41592-022-01507-1.

31. Urnavicius, L., C. K. Lau, …, A. P. Carter. 2018. Cryo-EM shows how dynactin recruits two dyneins for faster movement. *Nature.* 554:202–206. https://doi.org/10.1038/nature25462.

32. Berman, H. M., J. Westbrook, …, P. E. Bourne. 2000. The protein data bank. *Nucleic Acids Res.* 28:235–242. https://doi.org/10.1093/nar/28.1.235.

33. Garner, R. M., A. T. Molines, …, F. Chang. 2023. Vast heterogeneity in cytoplasmic diffusion rates revealed by nanorheology and Doppelgänger simulations. *Biophys. J.* 122:767–783. https://doi.org/10.1016/j.bpj.2023.01.040.

34. Boas, M. L. 1982. Mathematical methods in the physical sciences. Wiley, p. c1982, 1983.

35. Ananthanarayanan, V., M. Schattat, …, I. M. Tolić-Nørrelykke. 2013. Dynein motion switches from diffusive to directed upon cortical anchoring. *Cell.* 153:1526–1536. https://doi.org/10.1016/j.cell.2013.05.020.

36. Axelrod, D. 2001. Total internal reflection fluorescence microscopy in cell biology. *Traffic.* 2:764–774. https://doi.org/10.1034/j.1600-0854.2001.21104.x.

37. Cinelli, R. A., A. Ferrari, ..., F. Beltram. 2000. The enhanced green fluorescent protein as a tool for the analysis of protein dynamics and localization: local fluorescence study at the single-molecule level. *Photochem. Photobiol.* 71:771−776. https://doi.org/10.1562/0031-8655(2000)071<0771:tegfpa>2.0.co;2.

38. Johansen, A. M. 2010. Monte Carlo Methods. *In* International encyclopedia of education Elsevier, pp. 296−303.

39. Brouhard, G. J., and L. M. Rice. 2018. Microtubule dynamics: an interplay of biochemistry and mechanics. *Nat. Rev. Mol. Cell Biol.* 19:451−463. https://doi.org/10.1038/s41580-018-0009-y.